12th International Symposium on Turbulence and Shear Flow Phenomena (TSFP12)
Osaka, Japan, July 19–22, 2022

PARTICLE RESOLVED DNS STUDY OF TURBULENCE EFFECTS ON HYPORHEIC MIXING IN RANDOMLY PACKED SEDIMENT BEDS

Shashank K. Karra
School of Mechanical, Industrial, and Manufacturing Engineering
Oregon State University
Corvallis, OR 97331
karras@oregonstate.edu

Sourabh V. Apte
School of Mechanical, Industrial, and Manufacturing Engineering
Oregon State University
Corvallis, OR 97331
sourabh.apte@oregonstate.edu

Xiaoliang He
Pacific Northwest National Laboratory
Richland, WA 99354
xiaoliang.he@pnnl.gov

Timothy D. Scheibe
Pacific Northwest National Laboratory
Richland, WA 99354
tim.scheibe@pnnl.gov

ABSTRACT

Pore-resolved direct numerical simulations (DNS) are used to investigate the interactions between stream-water flow turbulence and groundwater flow through a porous sediment bed in the hyporheic zone. Two permeability Reynolds numbers (2.56 and 5.17), representative of aquatic systems and representing ratio of permeability to viscous length scales, were simulated to understand its influence on the momentum exchange at the sediment-water interface (SWI). A double-averaging methodology is used to compute the Reynolds stresses, form-induced stresses, and pressure fluctuations. It is observed that both shear layer and turbulent shear stress penetration increases with Re_K. Reynolds and form-induced bed-normal stresses increase with Re_K. The peak values of the form-induced stresses for the lower (2.56) and higher (5.17) Re_K happen within the top layer of the sediment bed. The sum of turbulent and form-induced pressure fluctuations, analyzed at their respective zero-displacement planes, are statistically similar and can be well approximated by a *t location-scale distribution* fit providing with a model that could potentially be used to impose boundary conditions at the SWI in reach scale simulations.

INTRODUCTION

The interchange of mass and momentum between surface water and ground water occurs in the porous bed beneath the streams, termed as the hyporheic zone. The exchange of mass and momentum (hyporheic exchange) of solutes such as chemicals and pollutants, dissolved oxygen, nutrients, and heat across this zone is a critical component in sustaining diverse aquatic ecosystems. The penetration of mean and turbulent flow within the porous bed and near bed pressure fluctuations have been identified (Hester *et al.* (2017)) to play a crucial in understanding this hyporheic exchange. While there are many parameters which characterize exchange of mass and momentum across the sediment water interface (SWI), the permeability Reynolds number, representing the ratio between the permeability scale to the viscous scale $\sqrt{K}/(\nu/u_\tau)$, is typically used to identify different flow regimes based on the dominant transport mechanisms across the SWI. Based on the characterization by Voermans *et al.* (2017, 2018); Grant *et al.* (2018) turbulence is dominant near the SWI for $Re_K > 1$ (figure 1a).

This study aims at using direct numerical simulations (DNS) to quantify the influence of varying Re_K on turbulent flow statistics near the SWI. Most of the prior experimental and numerical studies have been done at higher Re_k numbers ($10 < Re_K < 100$) with uniformly distributed sediment beds. Therefore this study aims at simulating turbulent flow over realistic randomly packed sediment bed arrangements with Re_K values ($1 < Re_K < 10$) found in typical aquatic beds. This study also aims at providing quantifiable data to improve the accuracy of reach-scale modeling, which use the mean pressure and turbulent kinetic energy distributions at the SWI, obtained from a RANS based surface flow simulation, as boundary conditions at the top surface of a ground-water flow model domain in a decoupled, sequential approach. In a previous study by the authors (Karra *et al.*, 2022), it was found that turbulent and pressure fluctuations are better captured by considering at least the top layer of sediment bed at lower Re_K numbers. In the current work this is found to be true even at higher Re_K numbers with turbulent fluctuations due to bed heterogeneity peaking in the top layer for both lower and higher Re_K values. Importantly, the pdfs of pressure fluctuations for both cases are found to be statistically similar, and well approximated by a fitted model, which can be used as a pressure boundary condition at the SWI in reach scale models.

The rest of the paper starts with description of the simulation setup, parameters and mathematical formulation used in the present work. A detailed description of the results and data analysis including validation against experimental data is then provided followed by summarizing the major findings of the present work.

SIMULATION DOMAIN AND PARAMETERS

The computational domain for the permeable sediment bed used in this study consists of a doubly periodic domain with four layers of randomly packed, mono-dispersed sediment grains at the bottom to capture the turbulence penetration

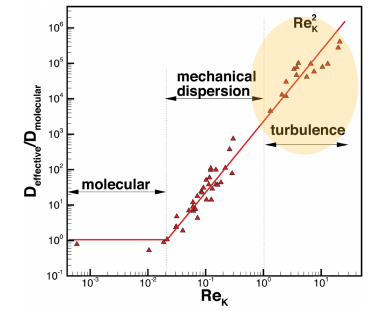

(a)

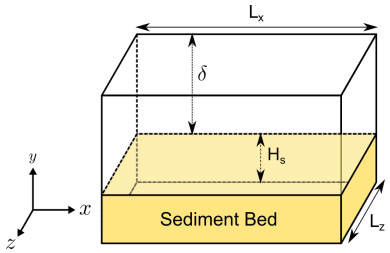

(b)

Figure 1. (a) Effective dispersion coefficient versus Re_k (based on Voermans *et al.* (2017); Grant *et al.* (2018)), (b) schematic of permeable bed showing height of roughness element layers, H_s, and boundary layer thickness, δ.

and unsteady, inertial flow (figure 2, Karra *et al.* (2020); Karra & Apte (2020)) . The random packing of mono-dispersed, spherical particles within a doubly periodic box is generated using the code developed by Dye *et al.* (2013).

Turbulent flow over a permeable bed can be characterized by the permeability Reynolds number (Re_K), the turbulent Reynolds number (Re_τ), the ratio of sediment depth to the free-surface height (H_s/δ), the ratio of the sediment grain diameter to the free-surface height (D_p/δ), bed porosity (θ), and the domain lengths in the axial and spanwise directions normalized by the free-surface height (L_x/δ, L_z/δ) (figure 1b). Table 1 shows detailed simulation parameters for the cases used to investigate the structure and dynamics of turbulence over porous sediment bed. Three permeable bed cases are simulated; case VV, case PBL, and case PBH. Case VV is used to verify and validate the DNS simulations of turbulent boundary layer flow over a sediment bed with experimental data from Voermans *et al.* (2017). Permeable bed case with porosity (θ) = 0.41, $Re_K = 2.56$ and $Re_\tau \sim 180$ match those of Case L12 in Voermans *et al.* (2017), and is within range for realistic aquatic sediments beds. Case PBL is simulated at lower Re_K value of 2.56 and case PBH is simulated at a higher Re_K value of 5.17.

The grid resolutions required for these configurations are based on two main considerations: (i) minimum bed-normal grid resolution near the bed, and (ii) minimum resolution required to capture flow over spherical particles. For DNS of boundary layers, the bed-normal grid resolution in wall units should be $\Delta y^+ < 1$, in order to accurately capture the bed shear stress in the turbulent flow. The grid resolutions in the axial and spanwise directions are typically 3–4 times coarser, following the smooth channel flow simulations by Moser *et al.* (1999). Note that, the roughness features and permeability are known to break the elongated flow structures along the axial direction in smooth walls, reducing the inhomogeneity in the near-bed region. This flow feature is thus anticipated to alleviate the bed-normal grid resolution requirement near the bed. To capture the inertial flow features within the pore and around

Table 1. Parameters used in present pore-resolved direct numerical simulations where, D_p is the sphere diameter, δ is the free surface height, H_s is the sediment depth, and θ is the porosity.

	VV	PBL	PBH
Re_K	2.56	2.56	5.17
Re_τ	180	270	540
θ	0.41	0.41	0.41
H_s/δ	1.71	1.14	1.14
D_p/δ	0.43	0.29	0.29
$(L_x, L_z)/\delta$	$(4\pi, 2\pi)$	$(4\pi, 2\pi)$	$(2\pi, \pi)$
$\Delta x^+ = \Delta z^+$	3.01	3.01	4.06
Δy^+	0.95	0.95	0.95

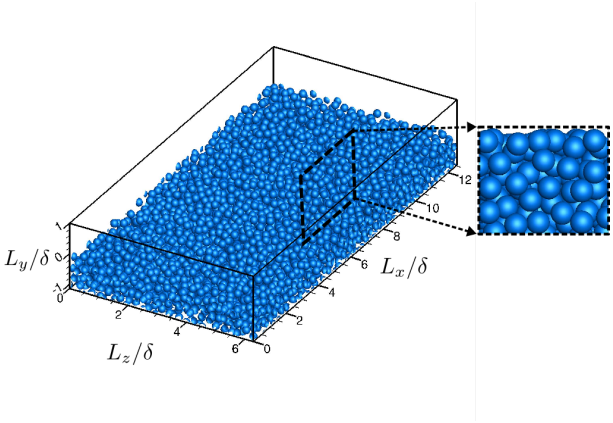

Figure 2. Permeable bed with four layers of sediment particles (inset shows close-up view in xy-plane)

spherical particles, grid refinement studies conducted on flow over single sphere (not shown) are used. Accordingly, roughly 180 grid points for the PBL case and 308 points for the PBH case are used in the bed-normal direction *within each sediment particle* in the top two layers. In the x and z directions, uniform grid with 26 and 38 grid points are used to resolve the grain geometry for the PBL and PBH cases, respectively.

Numerical scheme

The numerical approach is based on a fictitious domain method to handle arbitrary shaped immersed objects without requiring the need for body-fitted grids (Apte *et al.*, 2009). Cartesian grids are used in the entire simulation domain, including both fluid and solid phases. An additional body force is imposed on the solid part to enforce the rigidity constraint and satisfy the no-slip boundary condition. The absence of highly skewed unstructured mesh at the bead surface has been shown to accelerate the convergence and lower the uncertainty (Finn & Apte, 2013). The following governing equations are solved over the entire domain, including the region within the solid bed, and a rigidity constraint force, **f**, is applied that is non-zero only in the solid region. The governing

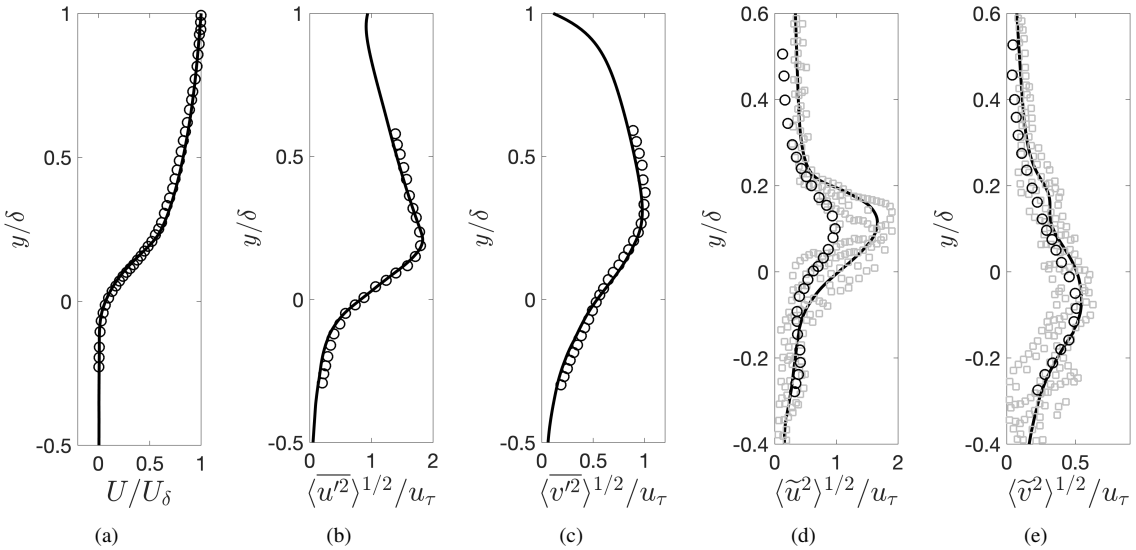

Figure 3. Comparison of (a) mean velocity and (b) streamwise, and (c) wall-normal components of Reynolds stress tensor, (d) streamwise and (e)wall-normal components of form-induced stress tensor. Experimental data by Voermans *et al.* (2017) (○), emulating experimental sampling (□), DNS (—).

equations are given as:

$$\nabla \cdot \mathbf{u} = 0, \tag{1}$$

$$\rho_f \left[\frac{\partial \mathbf{u}}{\partial t} + (\mathbf{u} \cdot \nabla)\,\mathbf{u} \right] = -\nabla p + \mu_f \nabla^2 \mathbf{u} + \mathbf{f} \tag{2}$$

where $\mathbf{u}$ is the velocity vector (with components given by $\mathbf{u} = (u_x, u_y, u_z)$, ρ_f the fluid density, μ_f the fluid dynamic viscosity, and p the pressure. A fully parallel, structured, collocated grid solver has been developed and thoroughly verified and validated for a range of test cases including flow over a cylinder and sphere for different Reynolds numbers, flow over touching spheres at different orientations, flow developed by an oscillating cylinder, among others. The details of the algorithm as well as very detailed verification and validation studies have been published (Apte *et al.*, 2009; Finn & Apte, 2013).

RESULTS

In this section validation of DNS simulations (VV case) is shown first followed by results for different Re_K cases, PBL and PBH.

Comparison with experimental data

Since the flow properties are highly spatially heterogeneous near rough sediments, double averaging procedure (Raupach & Thom, 1981) is used, wherein spatial averaging is performed along with time averaging,

$$\phi(x,t) = \langle \overline{\phi} \rangle(y) + \widetilde{\phi}(x) + \phi'(x,t) \tag{3}$$

where ϕ is an instantaneous flow variable, $\langle \phi \rangle$ is the intrinsic spatial average in the (x,z) plane, $\langle \phi \rangle = 1/A_f \int_{A_f} \phi dA$ (where A_f is the area occupied by the fluid), $\overline{\phi}$ is the temporal average, $\phi' = \phi - \overline{\phi}$ is the instantaneous turbulent fluctuation and $\widetilde{\phi} = \overline{\phi} - \langle \overline{\phi} \rangle$ is the form-induced or dispersive fluctuation. Accordingly, Reynolds stresses, form-induced stresses and , pressure fluctuations shown in this section are computed using the double averaging procedure.

Pore-resolved direct numerical simulations of turbulent boundary layer flow over a sediment bed were first validated with experimental data from Voermans *et al.* (2017). Permeable bed case with porosity of 0.41, $Re_K = 2.56$ and $Re_\tau \sim 180$ matches with Case L12 in Voermans *et al.* (2017),which is within the range for realistic aquatic sediments beds. For this validation study, the simulation domain used is same as in the DNS study of Shen *et al.* (2020).

The double-averaged (DA) mean velocity profile normalized by free-surface velocity U_δ is shown in figure 3a. Excellent agreement is seen between the DNS data and experimental measurements. Figures 3b, and 3c, show a comparison of DA turbulence intensities, namely stream-wise, and wall normal stresses. Again very good agreement between DNS and experiment is observed. The form-induced intensities or dispersive stresses normalized by u_τ are shown in figures 3d, and 3e. Upon initial observation, noticeable differences are observed between current DNS and experimental results for dispersive stresses which can be explained as follows. Firstly, as mentioned in the previous section, spatial averaging is carried out over an entire $x-z$ plane at a given y location for DNS results. While for the experimental data, spatial averaging was performed over three different spanwise locations over six different measurements. To quantify the differences in the sampling procedures between the experiments and DNS, the experimental sampling process is replicated in the DNS data whereby spatial averaging is carried out at a few finite uncorrelated spanwise locations and repeated over different streamwise locations. A family of curves, shown by grey squares, indicates the associated uncertainty in the processing of the experimental data. The averaged experimental and DNS data are within this scatter for all axial locations. Secondly, it is has been reported in literature Nikora *et al.* (2002); Fang *et al.* (2018) that the spanwise averaging is highly sensitive to the geometry at the sediment-water interface. For the present DNS, only the mean porosity of the randomly distributed arrangement of mono-dispersed spherical particles is matched with the experimental geometry. However, the exact sediment-grain distribution in the experiments is unknown and is likely

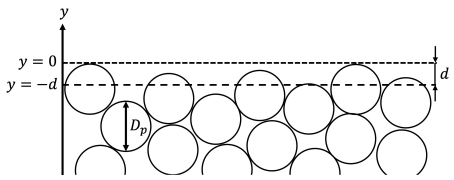

Figure 4. Schematic showing positions of sediment crest ($y = 0$), zero-displacement plane ($y = -d$), and particle diameter (D_p).

different compared to that used in DNS. This difference, especially near the top of the bed can also contribute to differences in the form-induced or dispersive stresses.

Zero-displacement plane and shear penetration

In turbulent flows over rough walls and permeable beds the log-law has the following form

$$\frac{U(y)}{u_\tau} = \frac{1}{\kappa}\log\left(\frac{y+d}{y_0}\right) \tag{4}$$

where κ is the von-Kármán constant, d is distance between the zero-displacement plane and the top of the sediment crest, and y_0 is the equivalent roughness height. Nikora *et al.* (2002) define d as the level that large-scale turbulent eddies feel as the bed origin and thus, their sizes linearly scale with distance from this level. The equivalent roughness height, y_0, is related to a measure of the size of the roughness elements. A schematic of the domain with the location of the sediment crest and the zero-displacement plane is shown in figure 4 where $y = 0$ is chosen at the sediment crest in the domain. For comparison of flow statistics between the PBL and PBH cases the virtual origin is chosen at the zero-displacement plane, $y = -d$. The fitting procedure (shown in Karra *et al.* (2022)) described by Breugem *et al.* (2006) is used to obtain the values of d and y_0 and are shown in table 2.

The depth of the shear layer penetration, known as the Brinkman layer thickness, δ_b, is defined as the vertical distance from the zero-displacement plane ($y = -d$) to the y location, inside the bed, which separates the constant or Darcy velocity region from the shear layer above it. Following the procedure by Voermans *et al.* (2017), δ_b is calculated as the y location (measured from $y = -d$) at which the difference between the local mean velocity and Darcy velocity, U_p, has decayed to 1% of the velocity value at the zero displacement plane, U_i, i.e $\langle\overline{u}\rangle(y)_{y+d=-\delta_b} - U_p = 0.01(U_i - U_p)$. Table 2 shows the δ_b values for both the PBL and PBH cases. Shear layer penetration increases Re_K and is of the same order as that of the sediment grain diameter for both cases.

The penetration depth of the turbulent shear stress into the bed, δ_p, defined as , $\langle\overline{u'v'}\rangle_{y=-\delta_p} = 0.01\langle\overline{u'v'}\rangle_i$, is shown in table 2. The value of δ_p increases with Re_K, even though the porosity of the beds for PBL and PBH cases remains the same.

Turbulence structure

Figures 5a,b show the streamwise and bed-normal Reynolds stresses for the PBL and PBH cases. The double-averaged variables are normalized by the friction velocity, u_τ^2 (pressure by ρu_τ^2), and y is shifted by d and then normalized by δ, effectively making virtual origin the same for both the cases. The axial component of turbulent velocity fluctuation, $\langle\overline{u'^2}\rangle^+$ (figure 5a), is greater for the PBL case than the PBH case. This is because at lower permeability Reynolds numbers, Re_K, the turbulent fluctuations into the wall (i.e., sweeps) are redirected into wall parallel components due to lower bed permeability. The bed-normal velocity fluctuations, $\langle\overline{v'^2}\rangle^+$, (figure 5b) for the PBH case are greater than the PBL case, and therefore increase with Re_K, suggesting both an increase in magnitude and penetration of flow turbulence into the sediment bed. The peak values for the Reynolds stresses, $\langle\overline{u'^2}\rangle^+$ and $\langle\overline{v'^2}\rangle^+$, happen very close to the sediment crest level and are shown in table 3. Compared to the PBH case the peak value of $\langle\overline{u'^2}\rangle^+$ and $\langle\overline{v'^2}\rangle^+$ for the PBL case is 11.9% greater and 12.8% lower.

Figures 5c,d show the bed-normal and shear form induced stresses and figure 5e shows the form-induced pressure fluctuations. Compared to the Reynolds stresses the peak value of form-induced stresses occurs significantly below the sediment crest. Similar to the Reynolds stress, the bed-normal form-induced stress, $\langle\widetilde{v}^2\rangle^+$, increases with Re_K, however the percentage increase is larger and the value of $\langle\widetilde{v}^2\rangle^+$ for PBH case is 47.9% greater than the PBL case, indicating that spatial heterogeneity at the roughness element length scale enhances both the turbulence intensity and penetration. The form-induced shear, $\langle\widetilde{u}\widetilde{v}\rangle^+$, also increases with Re_K, with the peak value for PBH case being 30% greater than the PBL case. In case PBH the form-induced stress has secondary peak in the free-stream region. These peaks in form-induced stresses have been reported by Fang *et al.* (2018) and are thought to be induced by time-averaged structure of secondary currents. Coleman *et al.* (2007) reported measuring these secondary currents in the free stream. They added these secondary current terms (namely, the integral from sediment crest to the free surface of, $\rho\langle\overline{w}\rangle\partial\langle\overline{u}\rangle/\partial z + \rho\langle\overline{v}\rangle\partial\langle\overline{u}\rangle/\partial y + \rho\partial\langle\overline{u'w'}\rangle/\partial z + \rho\partial\langle\widetilde{u}\widetilde{w}\rangle/\partial z$) to the total stress balance equation and highlighted their influence on momentum transfer. The peak value for form-induced pressure fluctuations, $\langle\widetilde{p}^2\rangle^+$, in the PBH case is 78.2% larger than the peak in PBL case. This is an important observation as it points to high sensitivity of spatial heterogeneity induced

Table 2. The von-Kármán constant (κ), zero-displacement thickness (d), and equivalent roughness height y_0 normalized by ν/u_τ. Brinkman-layer thickness (δ_b) and Reynolds-shear penetration depth are normalized by the free surface height δ.

Case	κ	d^+	y_0^+	δ_b/δ	δ_p/δ
PBL	0.32	47.0	6.65	0.197	0.382
PBH	0.31	96.0	8.87	0.248	0.44

Table 3. Peak value of normalized Reynolds and form-induced stresses for the PBL and PBH cases. Axial and bed-normal Reynolds stresses as well as the form-induced bed-normal, and shear stresses are normalized by u_τ^2, whereas the form-induced pressure fluctuations are normalized by ρu_τ^2.

Case	$\langle\overline{u'^2}\rangle^+$	$\langle\overline{v'^2}\rangle^+$	$\langle\widetilde{v}^2\rangle^+$	$\langle\widetilde{u}\widetilde{v}\rangle^+$	$\langle\widetilde{p}^2\rangle^+$
PBL	3.51	1.02	0.25	-0.21	3.69
PBH	3.09	1.17	0.48	-0.3	16.94

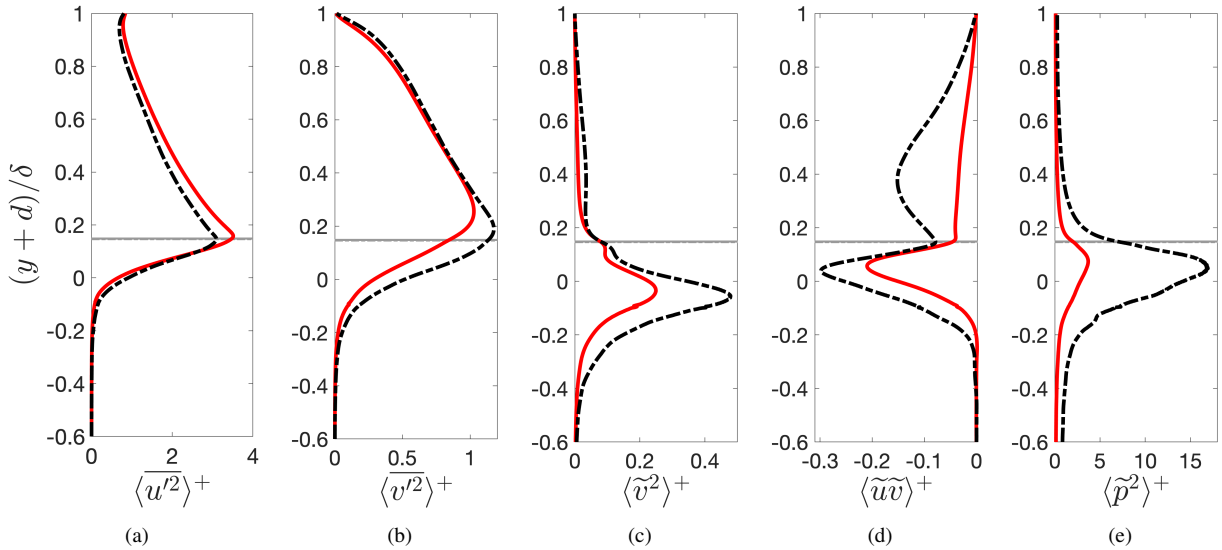

Figure 5. Comparison of Reynolds and form induced stress profiles for PBL (—) and PBH cases (- · -). (a) streamwise, and (b) wall-normal components of Reynolds stress tensor, (c) wall-normal and (d) shear stress components of form-induced stress tensor and (e) form-induced pressure fluctuations. Horizontal lines show the crest of sediment bed for PBL (—), and PBH (- · -) cases.

pressure fluctuations on Re_K. This increase in magnitude of pressure fluctuations at higher Re_K can result in decrease in particles/contaminants residence time inside the sediment bed. Most importantly, the form-induced stresses and pressure fluctuations peak within the top layer of the sediment bed for both low (2.56) and high (5.17) Re_K numbers. This further extends the observations reported by the authors in their prior work (Karra *et al.*, 2022), on the need to include atleast the top layer of the sediment bed in reach scale RANS models to better capture the influence of bed roughness on momentum exchange near the SWI to, higher Re_K numbers.

Turbulent pressure fluctuations

Pressure fluctuations at SWI play a critical role in hyporheic transport even for a flat bed. Specifically, pressure fluctuations due to turbulence are conjectured to have significant impact on mass transport within the hyporheic zone as it can directly influence the residence times through turbulent advection. Pressure fluctuation statistics for the PBL and PBH cases are compared at their respective zero-displacement planes, $y = -d$.

Figure 6a shows the pdfs of the sum of the turbulent, p', and form-induced, $\widetilde{p}$, pressure fluctuations normalized by their respective standard deviations for the PBL and PBH cases. The pdfs for both cases are statistically similar, closely approximating a normal distribution with heavier tails. This is a very important observation as this means that the pressure behavior inside the bed can be approximated with a model across a range of permeability Reynolds numbers, Re_K, which are typical for aquatic sediment beds. The pdf distributions in figure 6a was fitted with a *t location-scale distribution*, typically used for modeling data distributions with heavier tails. This model can be used as a boundary condition at the SWI in reach scale models. The parameters that define the *t location-scale distribution* model are the mean, μ, shape factor, ν, which can be understood as an estimator for skewness and kurtosis, and variance, defined using the standard deviation, σ and ν as $\frac{\sigma^2\nu}{\nu-2}$.

Figures 6b,c show the pdf distributions for the turbulent, p', and form-induced, $\widetilde{p}$, pressure fluctuations separately for both PBL and PBH cases. It can be observed that the pdf for turbulent fluctuations is closer to normal distribution behavior whereas the form-induced pressure fluctuations have skewed distributions showing how the bed surface variations influence local pressure distribution. Table 4 confirms that skewness, and kurtosis for $\widetilde{p}$ is higher than p'.

Table 4. Higher order statistics for turbulent and form induced pressure fluctuations, showing the mean $\mu(\cdot)$, standard deviation $\sigma(\cdot)$, skewness $Sk(\cdot)$, and kurtosis $Ku(\cdot)$.

	PBL	PBH
$\mu(\widetilde{p}+p')$, $\sigma(\widetilde{p}+p')$	-0.03, 2.77	-0.16, 13.0
$Sk(\widetilde{p}+p')$, $Ku(\widetilde{p}+p')$	0.75, 6.87	0.77, 6.67
$\mu(p')$, $\sigma(p')$	-0.13, 2.38	0.09, 10.64
$Sk(p')$, $Ku(p')$	-0.15, 5.25	-0.11, 7.27
$\mu(\widetilde{p})$, $\sigma(\widetilde{p})$	-0.03, 1.60	-0.16,7.28
$Sk(\widetilde{p})$, $Ku(\widetilde{p})$	1.70, 8.08	2.13, 10.21

CONCLUSIONS

Pore-resolved direct numerical simulations of turbulent boundary layer over a porous sediment bed were performed at two permeability Reynolds numbers (2.56 and 5.17). The key findings from these numerical experiments are summarized:

(i) The shear layer (Brinkman layer) thickness and turbulent shear stress penetration increase with Re_K and are on the order of the sediment grain diameter.

(ii) The Reynolds and form-induced stresses are influenced by the permeability Reynolds number, Re_K. The streamwise Reynolds stress peak value decreases with increase in Re_K whereas, the wall-normal Reynolds stress increases. Both bed-normal and shear form-induced stresses increase with Re_K. While the peak values for the Reynolds stresses happen

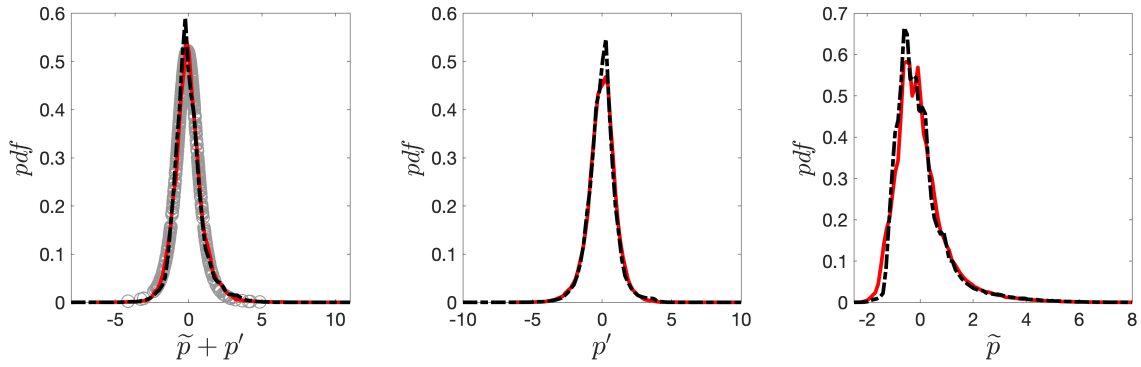

Figure 6. PDFs of (a) sum of turbulent p', and form-induced pressure fluctuations, $\widetilde{p}$ (the symbols (○) show the "*t location-scale distribution*" fit), (b) p' fluctuations and (c) $\widetilde{p}$ fluctuations. Legend: PBL (—) and PBH (- · -).

near the sediment crest, the form-induced stress peak values are observed inside the sediment bed. Importantly, the peak values of form-induced stresses, for both PBL and PBH cases, occur within the top layer of the sediment bed, highlighting the importance of including at least the top layer of the sediment bed in reach scale models to better capture the influence of bed roughness on momentum exchange near the SWI even at higher Re_K values.

(iii) The sum of turbulent and form-induced pressure fluctuations, analyzed at their respective zero-displacement planes, are statistically similar and can be well approximated by a *t location-scale distribution* fit. This is of critical importance as it can be potentially used as a boundary condition at the SWI in reach scale RANS simulations.

ACKNOWLEDGEMENTS

SVA and SKK gratefully acknowledge funding from US Department of Energy under award number DE-SC0021626 as well as US National Science Foundation award #205324. Frontera computing resources used under NSF's Leadership Resources Allocation (LRAC). XH and TDS acknowledge funding from the DOE Office of Biological and Environmental Research, Environmental System Science program, through the PNNL River Corridor Scientific Focus Area project (https://www.pnnl.gov/projects/river-corridor).

REFERENCES

Apte, S. V., Martin, M. & Patankar, N. A. 2009 A numerical method for fully resolved simulation (FRS) of rigid particle-flow interactions in complex flows. *Journal of Computational Physics* **228** (8), 2712–2738.

Breugem, WP, Boersma, BJ & Uittenbogaard, RE 2006 The influence of wall permeability on turbulent channel flow. *Journal of Fluid Mechanics* **562**, 35.

Coleman, SE, Nikora, Vladimir Ivanovich, McLean, SR & Schlicke, E 2007 Spatially averaged turbulent flow over square ribs. *Journal of engineering mechanics* **133** (2), 194–204.

Dye, Amanda L, McClure, James E, Miller, Cass T & Gray, William G 2013 Description of non-darcy flows in porous medium systems. *Physical Review E* **87** (3), 033012.

Fang, Hongwei, Xu, Han, He, Guojian & Dey, Subhasish 2018 Influence of permeable beds on hydraulically macro-rough flow. *Journal of Fluid Mechanics* **847**, 552–590.

Finn, Justin & Apte, Sourabh V 2013 Relative performance of body fitted and fictitious domain simulations of flow through fixed packed beds of spheres. *International journal of multiphase flow* **56**, 54–71.

Grant, Stanley B., Gomez-Velez, Jesus D. & Ghisalberti, Marco 2018 Modeling the effects of turbulence on hyporheic exchange and local-to-global nutrient processing in streams. *Water Resources Research* **54** (9), 5883–5889.

Hester, Erich T, Cardenas, M Bayani, Haggerty, Roy & Apte, Sourabh V 2017 The importance and challenge of hyporheic mixing. *Water Resources Research* **53** (5), 3565–3575.

Karra, Shashank K & Apte, Sourabh V 2020 Numerical investigation of high-speed oxy-fuel pulsed detonation for direct power extraction. In *ASME International Mechanical Engineering Congress and Exposition*, , vol. 84591, p. V011T11A002. American Society of Mechanical Engineers.

Karra, Shashank K, Apte, Sourabh V, He, Xiaoliang & Scheibe, Timothy D 2022 Pore-resolved simulations of turbulent boundary layer flow over permeable and impermeable sediment beds. *arXiv preprint arXiv:2204.13875* .

Karra, Shashank K, He, Xiaoliang, Apte, Sourabh, Scheibe, Timothy D, Richmond, Marshall C & Chen, Yunxiang 2020 Dns study of turbulence effects on hyporheic mixing in aquatic sediment beds. In *AGU Fall Meeting Abstracts*, , vol. 2020, pp. H086–0007.

Moser, Robert D, Kim, John & Mansour, Nagi N 1999 Direct numerical simulation of turbulent channel flow up to re τ= 590. *Physics of fluids* **11** (4), 943–945.

Nikora, Vladimir Ivanovich, Koll, K, McLean, SR, Ditrich, A & Aberle, J 2002 Zero-plane displacement for rough-bed open-channel flows. In *Fluvial Hydraulics River Flow 2002*, pp. 83–92.

Raupach, MR & Thom, A St 1981 Turbulence in and above plant canopies. *Annual Review of Fluid Mechanics* **13** (1), 97–129.

Shen, Guangchen, Yuan, Junlin & Phanikumar, Mantha S 2020 Direct numerical simulations of turbulence and hyporheic mixing near sediment–water interfaces. *Journal of Fluid Mechanics* **892**.

Voermans, JJ, Ghisalberti, M & Ivey, GN 2017 The variation of flow and turbulence across the sediment–water interface. *Journal of Fluid Mechanics* **824**, 413–437.

Voermans, Joey J, Ghisalberti, Marco & Ivey, Gregory N 2018 A model for mass transport across the sediment-water interface. *Water Resources Research* **54** (4), 2799–2812.